

Communication

Not peer-reviewed version

Phase Composition, Microstructure and Mechanical Properties of Vit-106 Alloy Obtained by Selective Laser Melting

[Roman Khmyrov](#)^{*}, Andrey Korotkov, Mikhail Gridnev, [Pavel Podrabinnik Podrabinnik](#), Tatiana Tarasova, [Andrey Gusarov](#)

Posted Date: 14 December 2023

doi: 10.20944/preprints202312.1032.v1

Keywords: bulk metallic glass; laser powder bed fusion; selective laser melting; Vit-106; amorphous alloys; additive manufacturing; crystallization; phase composition; mechanical properties.



Preprints.org is a free multidiscipline platform providing preprint service that is dedicated to making early versions of research outputs permanently available and citable. Preprints posted at Preprints.org appear in Web of Science, Crossref, Google Scholar, Scilit, Europe PMC.

Copyright: This is an open access article distributed under the Creative Commons Attribution License which permits unrestricted use, distribution, and reproduction in any medium, provided the original work is properly cited.

Communication

Phase Composition, Microstructure and Mechanical Properties of Vit-106 Alloy Obtained by Selective Laser Melting

Roman S. Khmyrov *, Andrey Korotkov, Mikhail Gridnev, Pavel Podrabinnik, Tatiana V. Tarasova and Andrey V. Gusarov

Laboratory of Innovative Additive Technologies, Moscow State University of Technology "STANKIN", Vadkovsky per. 1, 127055 Moscow, Russia; r.khmyrov@stankin.ru (R.S.Kh.); a.korotkov@stankin.ru (A.K.); gridnev.m@stankin.ru (M.G.); p.podrabinnik@stankin.ru (P.P.); t.tarasova@stankin.ru (T.V.T.); av.goussarov@gmail.com (A.V.G.)

* Correspondence: r.khmyrov@stankin.ru (R.S.Kh.)

Abstract: Vit-106 is a promising zirconium-based alloy with high glass-forming ability and belongs to the so-called bulk metallic glasses (BMG). Workpieces with a size of around one centimeter in all three dimensions can be obtained from a BMG alloy by casting. However, further increasing the cast size decreases the cooling rate and thus induces crystallization. Selective laser melting (SLM) is a well-known technique to overcome the size limitations for BMGs because a workpiece is built by the addition of multiple melt portions where the cooling rate is kept above the critical one. Currently, BMG parts obtained by SLM suffer from partial crystallization. The present work studies the influence of SLM process parameters on partial crystallization of Vit-106 by metallography and the influence of the microstructure on mechanical properties by microhardness and wear resistance testing. Submicron crystalline inclusions are observed in an amorphous matrix of Vit-106 alloy obtained by SLM. The size and the concentration of the inclusions can be controlled by varying the laser scanning speed. It is shown that submicron crystalline inclusions formed in the amorphous matrix during SLM can favorably affect microhardness and wear resistance.

Keywords: bulk metallic glass; laser powder bed fusion; selective laser melting; Vit-106; amorphous alloys; additive manufacturing; crystallization; phase composition; mechanical properties

1. Introduction

Today, amorphous metallic alloys, also known as bulk metallic glasses (BMG), attract much attention as recent works report on new ways of production, high mechanical properties such as tensile strength, proportional limit, hardness, good wear behavior and corrosion resistance of these [1–3]. For example, the American company "Liquidmetal" has patented a technology for the manufacture of products from BMGs for medicine and industrial needs [4]. However, the application of the BMG alloys is not widespread, especially as structural materials. These materials are very sensitive to cooling rates during casting, which is the main method for their production. Therefore, the size and shape of the amorphous metals are limited.

In contrast to casting, selective laser melting (SLM) technology provides high cooling rates combined with the capability of complex-shaped parts building, while the dimensions of parts are only limited to the working zone of a machine. Applying SLM for obtaining BMGs provoked great interest in the past ten years indicating the promising outlook for this research area [5–9]. Nevertheless, BMG alloys are difficult materials for laser processing as experimental works exposed partial crystallization of the obtained parts. However, according to Ouyang et al., the content of the crystalline phase could be controlled by processing parameters [10]. The authors observed the crystalline phase in the heat-affected zone of the iron-based BMG. Similar findings were described

for the zirconium-based BMGs. [11–14]. Further investigation revealed cracking of the iron-based BMGs during SLM resulting in poor strength, while zirconium-based ones were crack-free [9,16]. Due to high vitrification ability and crack resistance during laser processing zirconium alloys are found to be the most suitable for the SLM.

Pauly et al. experimentally proved that the SLM method can produce completely amorphous metal alloys with mechanical strength comparable to similar cast alloys [17]. Common examination of the printed Zr-based BMGs to prove their key properties include indentation and nanoindentation [5,11,18,19], compression tests [4,5,20], four-point bending [18,19], impact toughness and fatigue strength tests [19,20] and pin-on-disk wear behavior tests [5,18].

Of the known zirconium-based BMG alloys, the following commercial alloys have become widespread: Vit 1, Vit 106, Vit 106a and AMZ 4. The composition and basic thermal properties of these alloys are summarized in Table 1. In this table, the composition of the alloys is listed in atomic percentages.

Table 1. Composition and basic thermal properties of zirconium-based BMG alloys.

| | Zr, % | Ti, % | Cu, % | Be, % | Ni, % | Nb, % | Al, % | Glass transition temperature, K | Crystallization temperature, K | Melting point, K | Ref. |
|----------|-------|-------|-------|-------|-------|-------|-------|---------------------------------|--------------------------------|------------------|------|
| Vit 1 | 41.2 | 13.8 | 12.5 | 22.5 | 0 | 0 | 0 | 625 | 705 | 930 | [21] |
| Vit 106 | 57 | 0 | 15.4 | 0 | 12.6 | 5 | 10 | 672 | 738 | 1092 | [22] |
| Vit 106a | 58.5 | 0 | 15.6 | 0 | 12.8 | 2.8 | 10.3 | 668 | 772 | 1110 | [23] |
| AMZ 4 | 59.3 | 0 | 28.8 | 0 | 0 | 1.5 | 10.4 | 673 | 743 | 1203 | [24] |

Based on this table, it was decided that the use of Vit 1 alloy in the work is hazardous to health. There are similarities in composition and properties between Vit 106, Vit 106a and AMZ 4 alloys, so it was decided to choose a more accessible material for research. In our case, Vit 106 turned out to be the more accessible material.

Previous works revealed partial crystallization of the BMGs during SLM [25]. Research to date has not yet determined its influence on the properties of amorphous materials. Thus, this work aimed at studying the microstructure of the Vit-106 alloy after SLM and the influence of the features observed on the properties of the BMG material.

2. Materials and Methods

2.1. Materials

In total, 5 Vit-106 specimens were studied within this work. Specimen №1 was an as-received Vit-106 alloy plate. However, a defect layer is expected on the surface of the plate after casting in molds. Therefore specimen №2 was prepared by grinding an as-received plate on the depth of 30 μm. Specimen №3 is also a Vit-106 plate subjected to heat treatment in order to achieve full crystallization. Previous studies revealed the SLM process parameters that lead to partial crystallization of the Vit-106 alloy [25]. These parameters were used for the SLM production of two 5-layered specimens No. 4 and No. 5 with different laser scanning speeds V, laser power P, powder layer thickness H and hatch distance S (Table 2).

Table 2. Specimens specification.

| No. | Specimen | Description |
|-----|-------------------|---|
| 1 | Amorphous plate | As-received |
| 2 | Amorphous plate | Grinded plates to remove defect surface layers |
| 3 | Crystalline plate | Plate annealed at 700 °C for 2 hours in vacuum with 10 K/min heating and cooling rate |
| 4 | Multilayered SLM | P=160W, V=350 mm\s, S=185 μm, H = 70 μm, 5 layers |
| 5 | Multilayered SLM | P=160W, V=700 mm\s, S=125 μm, H = 70 μm, 5 layers |

To obtain crystalline Vit-106 specimens, amorphous plates were annealed in a Termionik T1 vacuum furnace (JSC Termionik, Podolsk, Russia). Powder for the SLM process was manufactured by milling an amorphous Vit-106 chip in distilled water in a planetary ball mill Retsch pm100 (Retsch, Haan, Germany). An amorphous Vit-106 chip was obtained by machining Vit-106 plates. The average size of powder particles was controlled by optic microscopy every 15 minutes. Because milling time is a key parameter that determines the size of powder particles. Short time results in coarse particles and a broad range of sizes while long milling leads to submicron particles. Therefore, an experimentally optimal time for powder production with an average particle size of 50 μm required for most SLM machines was found (Table 3). Since it is impossible to obtain a spherical shape by ball milling, irregularly shaped 20-50 μm powder was used in the current work. After milling, the powder was dried and sieved to provide a 20-50 μm particle size interval. Figure 1 demonstrates the prepared powder.

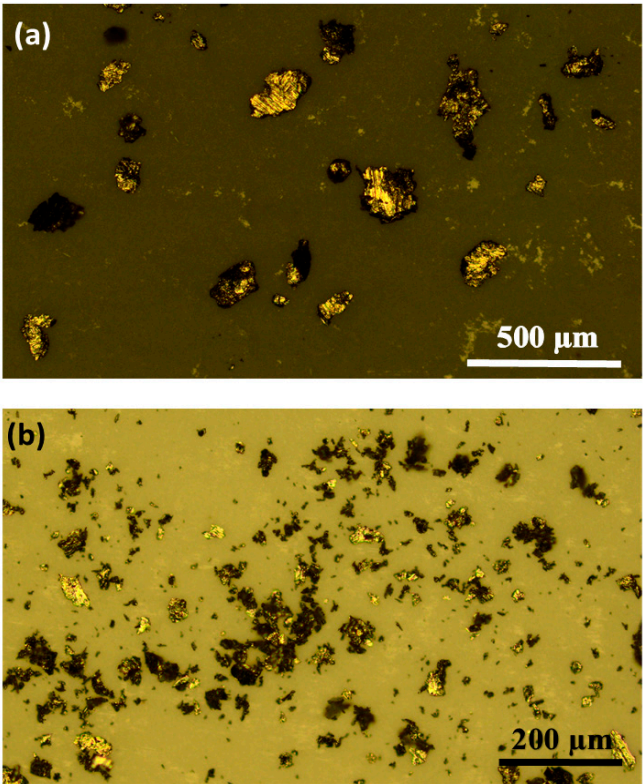


Figure 1. Vit-106 powder after milling: (a) 35 min. ball milling time; (b) after 100 min.

Table 3. Powder characterization after ball milling.

| | | | | |
|---------------------------|-----|-----|----|-----|
| Ball milling time, min | 35 | 50 | 75 | 100 |
| Average particle size, μm | 156 | 103 | 85 | 51 |
| Standard deviation, μm | 77 | 46 | 32 | 20 |

2.2. SLM

A Laboratory SLM rig was used to build multilayered specimens. The process took place in an argon atmosphere to prevent oxidation. Amorphous Vit-106 plates were used as a substrate. For the obtained samples, the scanning speed is as the only variable parameter, since it influences the cooling rate, and consequently the crystallization, more than the other parameters.

2.3. Characterization

The microstructure of the specimens was studied by optic microscopy Olympus BX 51 (Olympus Corp., Tokyo, Japan) and scanning electron microscopy Phenom ProX (Phenom-World BV, Eindhoven, The Netherlands). The chemical composition of the alloy $\text{Zr}_{59}\text{Cu}_{14.3}\text{Ni}_{11.9}\text{Al}_{9.3}\text{Nb}_{5.5}$ was confirmed by energy-dispersive analysis (EDX) in [25]. In addition, the content of oxygen was measured by the method of reductive melting of material in a helium flow using a Leco TC-600 analyzer (LECO Corporation, St. Joseph, MI, USA). The cross sections of the specimens were polished prior to studying. To increase the contrast for the optic microscopy, some cross sections were etched with a mixture of hydrofluoric and nitric acids. X-ray diffraction (XRD) analysis was used to determine the phase composition of the samples. XRD patterns were obtained by PANalytical Empyrean X-ray diffractometer with $\text{CuK}\alpha$ radiation. Phase composition analysis was performed by PANalytical High Score Plus software, software [26] and ICDD PDF-2 and COD databases [27].

Microhardness was measured by the indentation method with loads of 50 g and 500 g for 10 seconds using a Tykon 2500 microhardness tester (TUKON, Norwood, MA, USA). Each specimen was measured 9 times on the preliminary polished surface and cross section. The indentation was located 70 μm away from the edge.

Tribological pin-on-disk tests were performed on the Ducom tribometer (DUCOM, Bangalore, India) at the load of 10 N and sliding velocity 200 min^{-1} for 900 seconds. A ceramic 6 mm Al_2O_3 ball was used as a counterbody. The depth of the wear tracks was measured on the Hommel Tester 8000 profilograph (Jenoptik, Jena, Germany). The roughness of each specimen was measured in two perpendicular directions.

3. Results

3.1. Microstructure and phase composition

Figure 2 shows the cross sections of the specimens № 4 and № 5 at different magnifications. Common SLM microstructure features such as melt pool fragments are observed. Material flows are clearly seen in SEM images (Figure 3) which are attributed to high viscosity. Similar phenomena were found in silicon glasses subjected to SLM processing [28]. In contrast to specimen № 5, specimen № 4 had crystalline phases at the layer-substrate interface (Figure 3). It is possible that lower scanning speed V provoked the crystallization of the sublayers. In specimen № 4, coarser inclusions were detected at the boundary of the vortex (Figure 3 b, d, Zone I) than inside (Figure 3 b, d, Zone I). Meanwhile, specimens № 4 had areas free from such inclusions. In addition, Zone III with clear white inclusions around black ones was distinguished in Figure 3 b. Being bright, the inclusions presumably are lighter phases with deterioration of aluminum. Specimen № 5 demonstrated no such precipitations as dark inclusions were surrounded by homogenous grey areas. Dark areas observed in the microstructure are presumably either the intermetallic Al inclusions or oxide crystals as raw material contains 0.058 % wt. of oxygen.

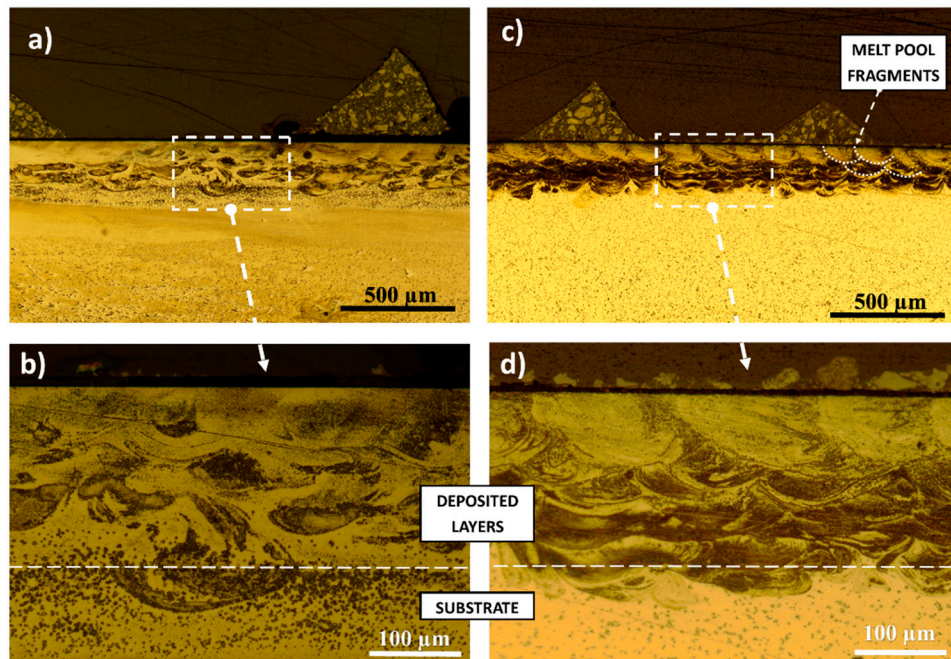


Figure 2. The cross sections of the specimens (a, b) No. 4 and (c, d) No. 5.

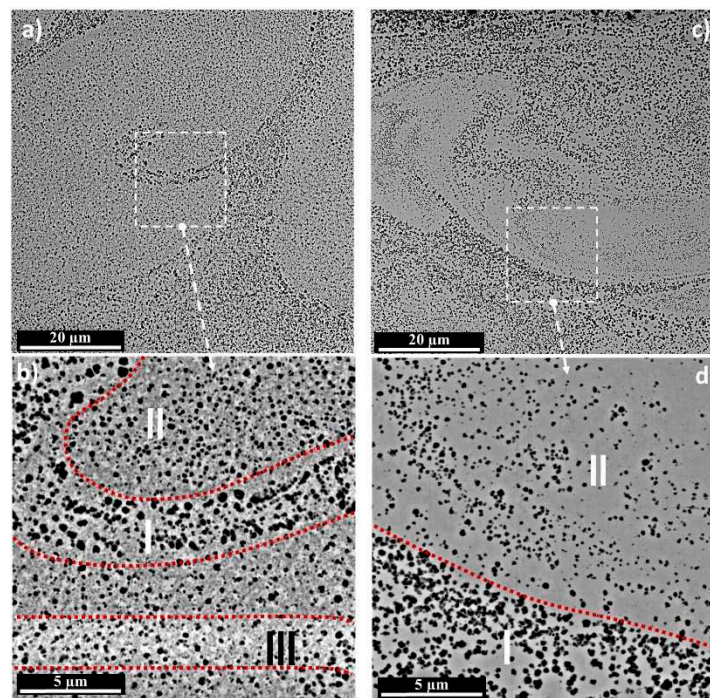


Figure 3. The SEM images of the specimens (a, b) No. 4 and (c, d) No. 5.

Figure 4 shows the XRD patterns of the raw alloy, powder and specimens № 3-5. Powder and raw plate share a very similar profile indicating that both materials are in an amorphous state. After annealing the material became crystalline as the “amorphous halo” was no longer observed. Multilayered specimens were found to be partially crystallized as the “amorphous halo” appeared as a smooth part of the curve with its highest intensity at $2\theta=39^\circ$. Along with that peaks identified as Zr_3O and Al, Zr and Cu intermetallic compounds were revealed. Therefore, the obtained specimens were partially crystalline.

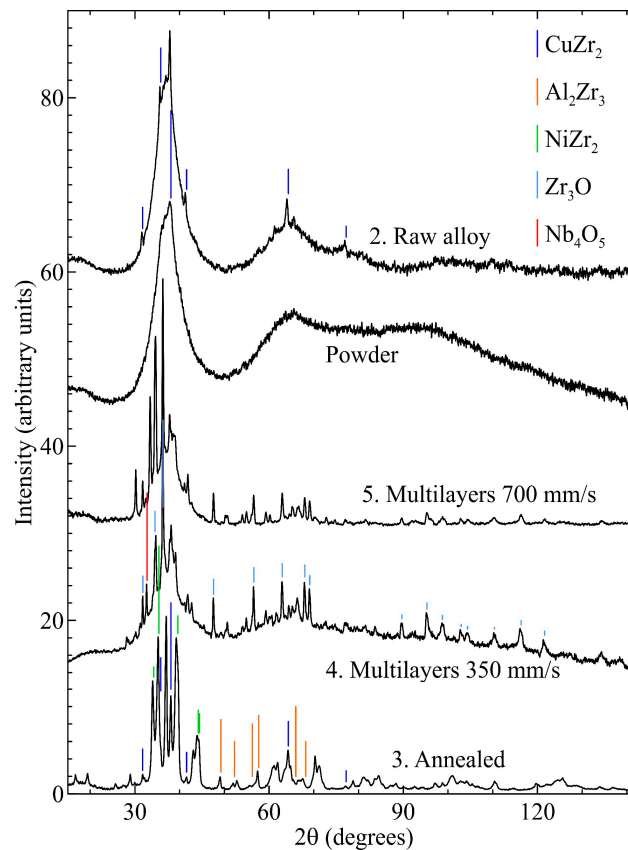


Figure 4. The XRD patterns of the specimens. Marks indicate peaks of possible crystalline phases.

3.2. Mechanical and tribological properties

Figure 5 shows the results of the microhardness tests on the surface of the specimens at 50 g and 500 g. Since no significant difference between the results of the specimens № 1 and № 3 was observed the 50 g tests for specimen № 2 were not performed. Microhardness of the cross sections was measured only for the multilayered specimens made from powder (figure 6). The highest value of 883 HV was demonstrated by the annealed crystalline plate, while the lowest (530 HV) value was measured for the raw amorphous alloy. The microhardness of the SLM specimens was closer to the amorphous ones. Being obtained at the fastest scanning speed, specimen № 5 had the closest to amorphous state hardness value. This may be attributed to the size of crystalline inclusions that grow at low scanning speeds and, hence, low cooling rates [29]. The hardness results of the fully crystalline specimen № 3 showed a large mean square deviation which was possible due to the size of the crystalline phase which can be comparable to the indentation size (figure 7). The deviation range reduces with the growth of load which increases the size of the dint and averages the contribution of the main material and crystalline inclusions.

The results of tribological tests and roughness measurements are given in Table 4. Average roughness is neglectable comparing to a wear track depth and it did not affect the results. The maximum profile depth was measured as shown in Figure 8.

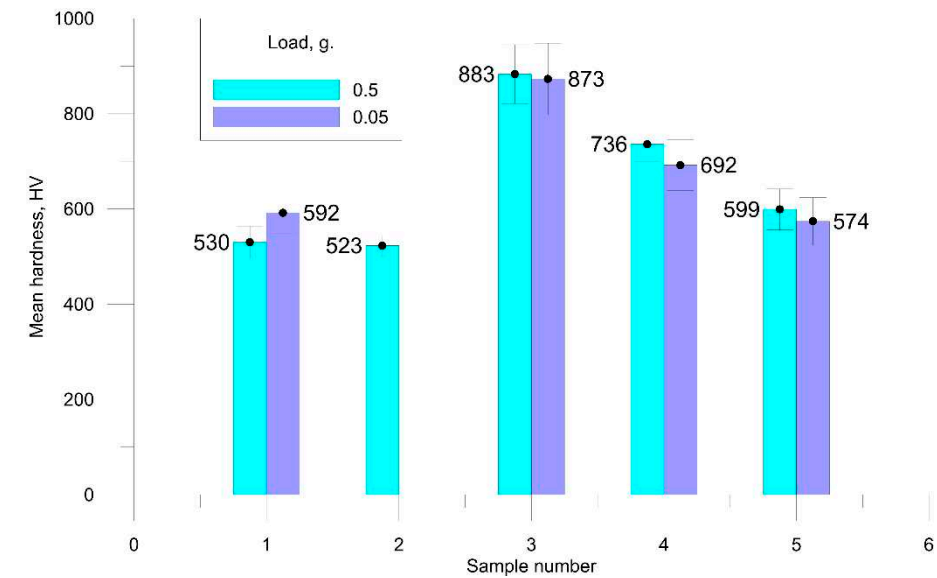


Figure 5. The results of the surface hardness tests.

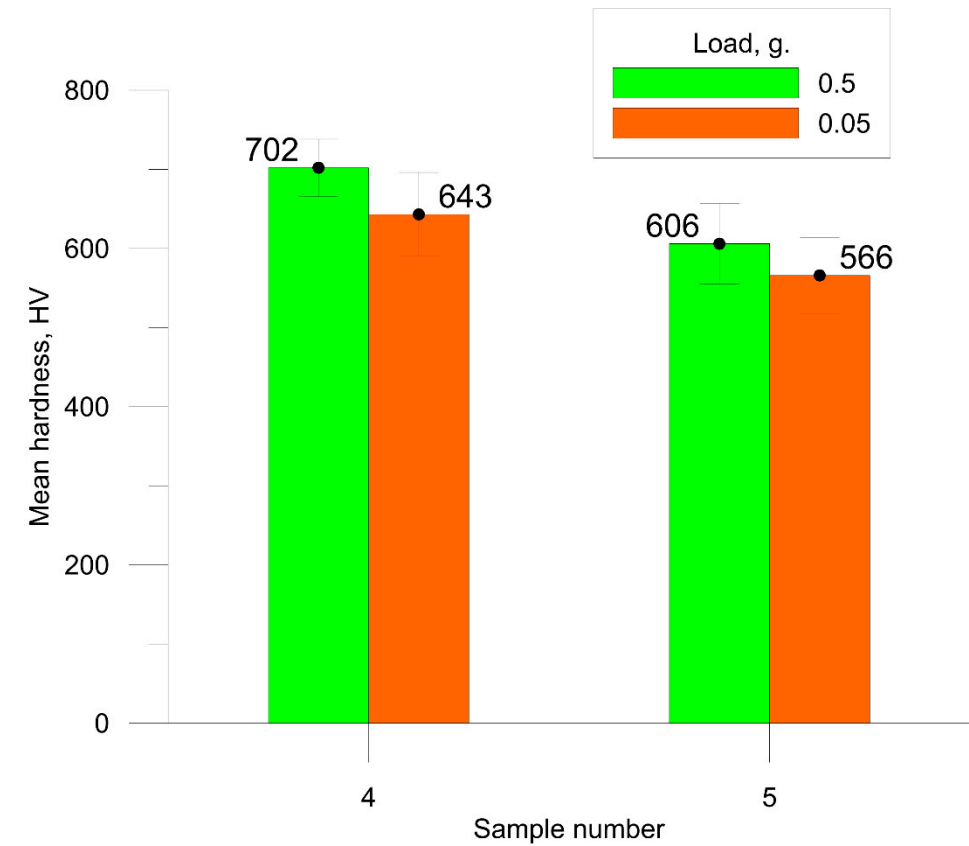


Figure 6. The results of the cross section hardness tests.

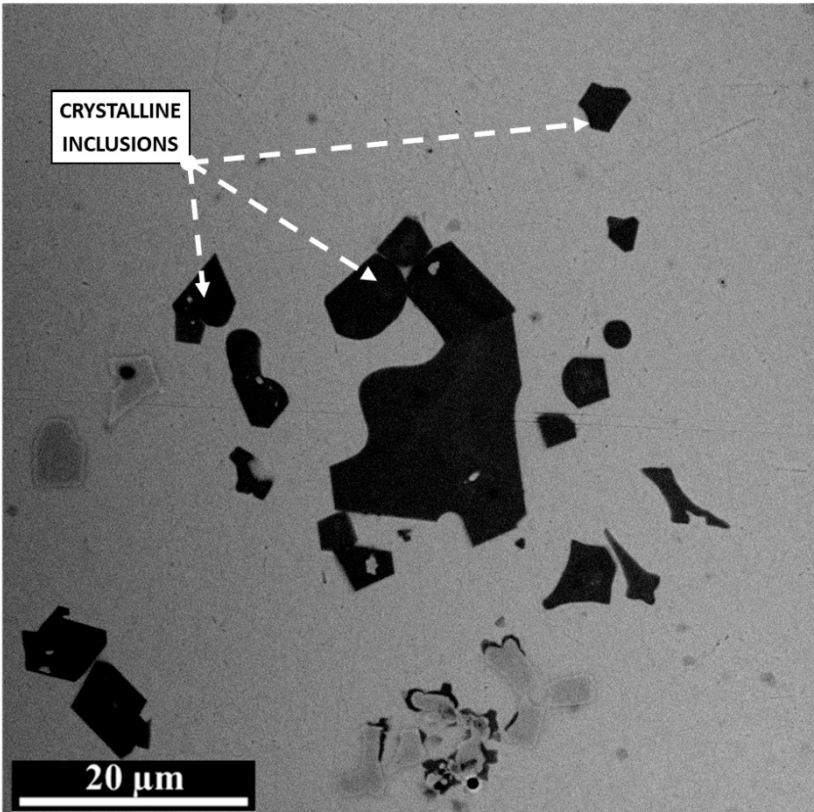


Figure 7. The microstructure of the specimen № 3.

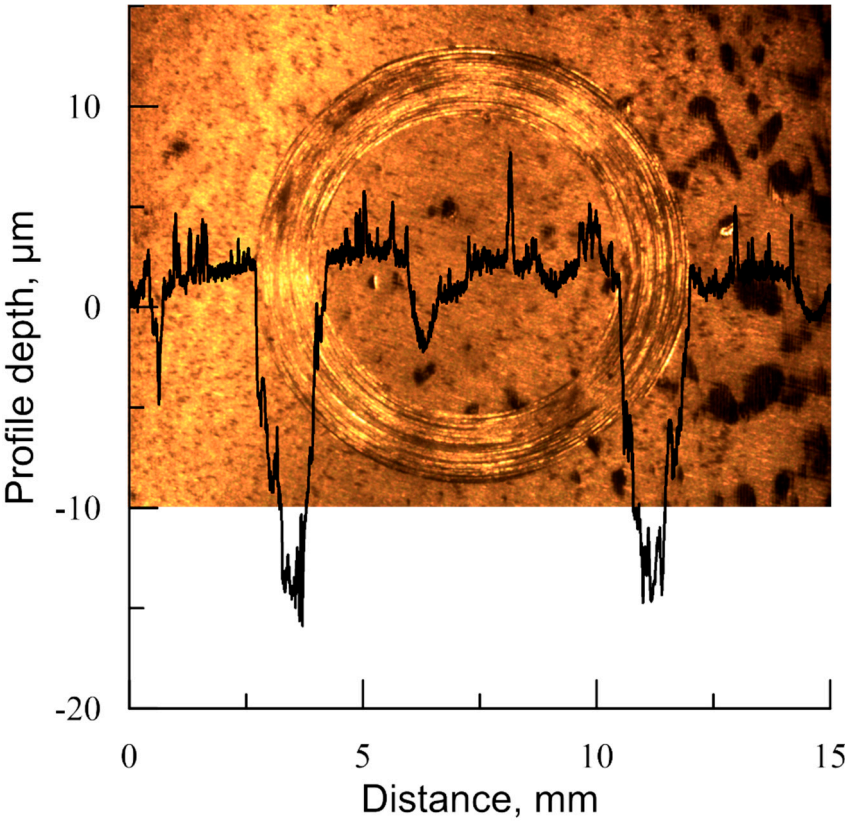


Figure 8. Wear track of the specimen № 5 with the overlaid profile.

Table 4. The results of wear tests.

| Specimen No. | Max. wear track depth, μm | The coefficient of friction | Surface roughness, $R_a, \mu\text{m}$ | Surface roughness, $R_z, \mu\text{m}$ |
|--------------|--------------------------------------|-----------------------------|---------------------------------------|---------------------------------------|
| 1 | 33 | 0.5 | 0.684 | 4.351 |
| 3 | 28 | 0.7 | 0.272 | 2.134 |
| 4 | 19 | 0.52 | 0.533 | 2.950 |
| 5 | 17 | 0.5 | 0.310 | 4.237 |

4. Discussion

The obtained multilayered SLM specimens №4 and №5 consisted of an amorphous matrix with crystalline inclusions that spread inhomogeneously and formed a vortex structure. Lower scanning speed $V=350\text{ mm/s}$ resulted in coarser inclusions in the substrate-alloy interface and vortexless structure (Figure 2b). The vortices in the remelted zone were measured to be around $100\text{ }\mu\text{m}$ (Figure 2 b, d), which corresponds to melt pool size under these conditions [21]. It can be suggested that either crystalline inclusions or their nuclei are transported by convective melt flows. The surface of the melt material could serve as the source for the nucleates given that a small content of oxides is expected due to residual oxygen in the shield gas. Oxidation was earlier reported to provoke crystallization in Zr-based BMGs [30]. Zr_3O and other oxides were found in the specimens studied within this work (Figure 5).

Dark inclusions in BSE SEM figures are presumably enriched with light elements which may be attributed to the oxides (Figure 3), Meanwhile, there is a bright halo around the inclusions which suggests the deterioration of the matrix with light elements (Figure 3 b, d). Thus, it can be concluded that during solidification the inclusions grow due to the diffusion of light elements from the matrix to them. The list of such elements includes oxygen dissolved in the matrix and lighter elements of the alloy Al, Ni, Cu, that form CuZr_2 intermetallic compound in raw material and Al_2Zr_3 и NiZr_2 compounds after annealing (Figure 4). However, the corresponding intermetallic lines of the specimens are not clear in the XRD patterns (Figure 4). Therefore, the observed inclusions mainly consist of ZrO_3 .

The inclusions in the remelted zone are submicron, and the higher the laser scanning speed the smaller the inclusions (Figure 3 b, d). The number of inclusions per unit area also decreases. It follows the model for homogeneous nucleation and nuclei growth. Indeed, the cooling rate increases with accelerating the laser scanning speed during solidification which reduces the time of homogeneous nucleation and inclusions grow. Therefore, the concentration and the size of the inclusions are anticipated to be smaller.

An amorphous plate with CuZr_2 intermetallides was taken for the multilayered specimens 4 and 5 [21]. These inclusions are observed in the nontreated area in Figure 3 a, c. Part of the substrate material close to the remelted layers is exposed to repeated thermal effects of a laser beam which may cause the growth of these inclusions. This is evidenced by the increased volume of the CuZr_2 particles (Figure 3b). The size of the typical inclusion reaches $20\text{ }\mu\text{m}$ (Figure 7). Higher laser scanning speed increases the cooling rate reducing the time of thermal exposure in the range where intensive crystal growth is possible. Therefore, faster scanning speed results in less intense growing of the inclusions.

The coefficient of friction (CoF) of the multilayered specimens remained almost the same as the raw material. At the same time, the wear track depth was significantly less indicating the positive influence of the submicron crystalline inclusions on wear resistance. Interestingly, that wear resistance slightly improves with increasing laser scanning speed from 350 mm/s to 700 mm/s . Obviously, smaller inclusions are beneficial for better wear resistance.

The microhardness of the SLM specimens was found to be higher than for raw material (Figure 6). This is also explained by the strengthening effect of submicron crystalline inclusions. At the same time, with increasing scanning speed, the microhardness decreases slightly. This trend is opposite to the effect of scanning speed on wear resistance and may be due to a decrease in the volume fraction of the crystalline phase with increasing scanning speed.

The results obtained show that submicron crystalline inclusions formed in an amorphous matrix during SLM can favorably affect mechanical properties such as microhardness and wear resistance. Correlations were revealed between these properties and such structural parameters as size, concentration and volume fraction of inclusions. The influence of such an important process parameter as scanning speed on the forming amorphous-crystalline structure is also shown. All these results can find practical application in the manufacture of structural elements from Zr-based BMG using SLM. At the same time, further systematic study of the influence of oxygen content in the starting material and possible partial oxidation from the gas phase on the forming microstructure, as well as the influence of microstructure on properties, is required.

Table 4. The results of wear tests.

| Specimen No. | Max. wear track depth, μm | The coefficient of friction | Surface roughness, R_a , μm | Surface roughness, R_z , μm |
|--------------|--------------------------------------|-----------------------------|--|--|
| 1 | 33 | 0.5 | 0.684 | 4.351 |
| 3 | 28 | 0.7 | 0.272 | 2.134 |
| 4 | 19 | 0.52 | 0.533 | 2.950 |
| 5 | 17 | 0.5 | 0.310 | 4.237 |

5. Conclusions

- Within this study, multilayered SLM specimens from Vit-106 were obtained, their microstructure was investigated, microhardness and tribological behavior were tested.
- The SLM specimens consisted of an amorphous matrix with two types of crystalline inclusions. Submicron CuZr_2 particles were found in the remelted vortex structure, while coarser up to $20 \mu\text{m}$ CuZr_2 were observed in the heat-affected zone of the substrate. The nature of the distribution of submicron inclusions shows that they can grow from oxide nuclei transported by convection in the melt pool.
- Large crystals in the thermally affected zone are most likely formed during the growth of intermetallic inclusions initially contained in the substrate material.
- Submicron crystalline inclusions increase wear resistance and can increase microhardness. The role of oxygen in the formation of the amorphous-crystalline structure, as well as the influence of structural parameters on mechanical properties requires further research.

Author Contributions: Conceptualization, A.V.G. and R.S.Kh.; methodology, R.S.Kh.; software, M.G.; validation, A.V.G., T.V.T and P.P.; formal analysis, P.P.; investigation, R.S.Kh., A.K., M.G.; resources, M.G.; data curation, P.P.; writing—original draft preparation, R.S.Kh., A.V.G.; writing—review and editing, P.P.; visualization, A.K.; supervision, R.S.Kh.; project administration, A.V.G.; funding acquisition, A.V.G. All authors have read and agreed to the published version of the manuscript.

Funding: This work was supported by the Russian Science Foundation (Grant Agreement No. 21-19-00295, <https://rscf.ru/project/21-19-00295/>).

Data Availability Statement: Data supporting the reported results can be found from the authors.

Acknowledgments: The study was carried out on the equipment of the Center of Collective Use “State Engineering Center” of the MSUT “STANKIN” (project 075-15-2021-695, unique id RF----2296.61321X0013).

Conflicts of Interest: The authors declare no conflict of interest.

References

1. Schuh, C.; Hufnagel, T.; Ramamurty, U. Mechanical Behavior of Amorphous Alloys. *Acta Mater.* **2007**, *55* (12), 4067–4109. DOI:10.1016/j.actamat.2007.01.052.
2. Greer, A. L. Metallic Glasses...on the Threshold. *Mater. Today* **2009**, *12* (1–2), 14–22. DOI:10.1016/s1369-7021(09)70037-9.
3. Kruzic, J. J. Bulk Metallic Glasses as Structural Materials: A Review. *Adv. Eng. Mater.* **2016**, *18* (8), 1308–1331. DOI:10.1002/adem.201600066.
4. <https://liquidmetal.com/> (accessed 2023-11-09).

5. Deng, L.; Gebert, A.; Zhang, L.; Chen, H. Y.; Gu, D. D.; Kühn, U.; Zimmermann, M.; Kosiba, K.; Pauly, S. Mechanical Performance and Corrosion Behaviour of Zr-Based Bulk Metallic Glass Produced by Selective Laser Melting. *Mater. Des.*, **2020**, *189*, 108532. DOI:10.1016/j.matdes.2020.108532.
6. Marattukalam, J. J.; Pacheco, V.; Karlsson, D.; Riekehr, L.; Lindwall, J.; Forsberg, F.; Jansson, U.; Sahlberg, M.; Hjärvarsson, B. Development of Process Parameters for Selective Laser Melting of a ZR-Based Bulk Metallic Glass. *Addit. Manuf.*, **2020**, *33*, 101124. DOI:10.1016/j.addma.2020.101124.
7. Lindwall, J.; Pacheco, V.; Sahlberg, M.; Lundbäck, A.; Lindgren, L.-E. Thermal Simulation and Phase Modeling of Bulk Metallic Glass in the Powder Bed Fusion Process. *Addit. Manuf.*, **2019**, *27*, 345–352. DOI:10.1016/j.addma.2019.03.011.
8. Jiang, Q.; Liu, H.; Li, J.; Yang, D.; Zhang, Y.; Yang, W. Atomic-Level Understanding of Crystallization in the Selective Laser Melting of FE50NI50 Amorphous Alloy. *Addit. Manuf.*, **2020**, *34*, 101369. DOI:10.1016/j.addma.2020.101369.
9. Bacheeva, A. V.; Khmyrov, R. S.; Korotkov, A. D.; Tarasova, T. V.; Gusarov, A. V. Amorphous-Crystalline Composite Microstructure Formation in Zr46Cu46al8 Alloy at the Conditions of Selective Laser Melting. *Key Eng. Mater.*, **2022**, *910*, 959–965. DOI:10.4028/p-1s59b9.
10. Ouyang, D.; Xing, W.; Li, N.; Li, Y.; Liu, L. Structural Evolutions in 3D-Printed FE-Based Metallic Glass Fabricated by Selective Laser Melting. *Addit. Manuf.*, **2018**, *23*, 246–252. DOI:10.1016/j.addma.2018.08.020.
11. Yang, G.; Lin, X.; Liu, F.; Hu, Q.; Ma, L.; Li, J.; Huang, W. Laser Solid Forming ZR-Based Bulk Metallic Glass. *Intermetallics*, **2012**, *22*, 110–115. DOI:10.1016/j.intermet.2011.10.008.
12. Zhang, Y.; Lin, X.; Wang, L.; Wei, L.; Liu, F.; Huang, W. Microstructural Analysis of ZR55CU30AL10NI5 Bulk Metallic Glasses by Laser Surface Remelting and Laser Solid Forming. *Intermetallics*, **2015**, *66*, 22–30. DOI:10.1016/j.intermet.2015.06.007.
13. Li, X. P.; Kang, C. W.; Huang, H.; Zhang, L. C.; Sercombe, T. B. Selective Laser Melting of an Al86ni6y4.5co2la1.5 Metallic Glass: Processing, Microstructure Evolution and Mechanical Properties. *Mater. Sci. Eng. A*, **2014**, *606*, 370–379. DOI:10.1016/j.msea.2014.03.097.
14. Li, X. P.; Roberts, M. P.; O’Keeffe, S.; Sercombe, T. B. Selective Laser Melting of ZR-Based Bulk Metallic Glasses: Processing, Microstructure and Mechanical Properties. *Mater. Des.*, **2016**, *112*, 217–226. DOI:10.1016/j.matdes.2016.09.071.
15. Li, N.; Zhang, J.; Xing, W.; Ouyang, D.; Liu, L. 3D Printing of Fe-Based Bulk Metallic Glass Composites with Combined High Strength and Fracture Toughness. *Mater. Des.*, **2018**, *143*, 285–296. DOI:10.1016/j.matdes.2018.01.061.
16. Marattukalam, J. J.; Pacheco, V.; Karlsson, D.; Riekehr, L.; Lindwall, J.; Forsberg, F.; Jansson, U.; Sahlberg, M.; Hjärvarsson, B. Development of Process Parameters for Selective Laser Melting of a ZR-Based Bulk Metallic Glass. *Addit. Manuf.*, **2020**, *33*, 101124. DOI:10.1016/j.addma.2020.101124.
17. Pauly, S.; Schricker, C.; Scudino, S.; Deng, L.; Kühn, U. Processing a Glass-Forming ZR-Based Alloy by Selective Laser Melting. *Mater. Des.*, **2017**, *135*, 133–141. DOI:10.1016/j.matdes.2017.08.070.
18. Bordeenithikaseem, P.; Stolpe, M.; Elsen, A.; Hofmann, D. C. Glass Forming Ability, Flexural Strength, and Wear Properties of Additively Manufactured ZR-Based Bulk Metallic Glasses Produced through Laser Powder Bed Fusion. *Addit. Manuf.*, **2018**, *21*, 312–317. DOI:10.1016/j.addma.2018.03.023.
19. Best, J. P.; Ostergaard, H. E.; Li, B.; Stolpe, M.; Yang, F.; Nomoto, K.; Hasib, M. T.; Muránsky, O.; Busch, R.; Li, X.; Kruzic, J. J. Fracture and Fatigue Behaviour of a Laser Additive Manufactured ZR-Based Bulk Metallic Glass. *Addit. Manuf.*, **2020**, *36*, 101416. DOI:10.1016/j.addma.2020.101416.
20. Best, J. P.; Ast, J.; Li, B.; Stolpe, M.; Busch, R.; Yang, F.; Li, X.; Michler, J.; Kruzic, J. J. Relating Fracture Toughness to Micro-Pillar Compression Response for a Laser Powder Bed Additive Manufactured Bulk Metallic Glass. *Mater. Sci. Eng. A*, **2020**, *770*, 138535. DOI:10.1016/j.msea.2019.138535.
21. Hays, C. C.; Kim, C. P.; Johnson, W. L. Large Supercooled Liquid Region and Phase Separation in the Zr–Ti–Ni–Cu–Be Bulk Metallic Glasses. *Applied Physics Letters* 1999, *75* (8), 1089–1091. DOI:10.1063/1.124606.
22. Dong, W.; Zhang, H.; Sun, W.; Ding, B.; Hu, Z. Formation, Thermal Stability and Mechanical Properties of Zr–Nb–Cu–Ni–Al Bulk Metallic Glasses. *MATERIALS TRANSACTIONS* 2006, *47* (5), 1294–1298. DOI:10.2320/matertrans.47.1294.
23. The Online Materials Information Resource. <http://www.matweb.com/search/datasheet.aspx?matguid=5c9ee48e2a704449b5880173789349cb&ckc k=1> (accessed 2023-12-08).
24. Marattukalam, J. J.; Pacheco, V.; Karlsson, D.; Riekehr, L.; Lindwall, J.; Forsberg, F.; Jansson, U.; Sahlberg, M.; Hjärvarsson, B. Development of Process Parameters for Selective Laser Melting of a ZR-Based Bulk Metallic Glass. *Additive Manufacturing* 2020, *33*, 101124. DOI:10.1016/j.addma.2020.101124.
25. Khmyrov, R. S.; Podrabinnik, P. A.; Tarasova, T. V.; Gridnev, M. A.; Korotkov, A. D.; Grigoriev, S. N.; Kurmysheva, A. Yu.; Kovalev, O. B.; Gusarov, A. V. Partial Crystallization in a Zr-Based Bulk Metallic Glass in Selective Laser Melting. *Int. J. Adv. Manuf. Technol.*, **2023**, *126* (11–12), 5613–5631. DOI:10.1007/s00170-023-11500-3.

26. Shelekhov, E. V.; Sviridova, T. A. Programs for X-Ray Analysis of Polycrystals. *Metal Sci. Heat Treat*, **2000**, 42(8), 309–313. DOI:10.1007/bf02471306.
27. Gražulis, S.; Chateigner, D.; Downs, R. T.; Yokochi, A. F.; Quirós, M.; Lutterotti, L.; Manakova, E.; Butkus, J.; Moeck, P.; Le Bail, A. Crystallography Open Database – an Open-Access Collection of Crystal Structures. *J. Appl. Cryst.*, **2009**, 42(4), 726–729. DOI:10.1107/s0021889809016690.
28. Grigoriev, S. N.; Khmyrov, R. S.; Gridnev, M. A.; Tarasova, T. V.; Gusarov, A. V. Optimizing the Process Parameters for Additive Manufacturing of Glass Components by Selective Laser Melting: Soda-Lime Glass versus Quartz Glass. *J. Manuf. Sci. Eng.*, **2021**, 144(6). DOI:10.1115/1.4052840.
29. Gridnev, M.; Khmyrov, R. S. Model of Heat Transfer and Crystallization Kinetics in the Heat-Affected Zone in VIT 106 Alloy in Selective Laser Melting. *High Temp. Mater. Process.*, **2023**. DOI:10.1615/hightempmatproc.2023048119.
30. Yang, Z.; Al-Mukadam, R.; Stolpe, M.; Markl, M.; Deubener, J.; Körner, C. Isothermal Crystallization Kinetics of an Industrial-Grade ZR-Based Bulk Metallic Glass. *J. Non-Cryst. Solids.*, **2021**, 573, 121145. DOI:10.1016/j.jnoncrysol.2021.121145.

Disclaimer/Publisher's Note: The statements, opinions and data contained in all publications are solely those of the individual author(s) and contributor(s) and not of MDPI and/or the editor(s). MDPI and/or the editor(s) disclaim responsibility for any injury to people or property resulting from any ideas, methods, instructions or products referred to in the content.